Published in final edited form as:
J Control Release. 2012 February 28; 158(1): 148–155. doi:10.1016/j.jconrel.2011.10.021.

Rapid tumoritropic accumulation of systemically injected plateloid particles and their biodistribution

Anne L. van de Ven[1,♣], **Pilhan Kim**[2,7], **O'Hara Haley**[2], **Jean R. Fakhoury**[1], **Giulia Adriani**[1,3], **Jeffrey Schmulen**[1], **Padraig Moloney**[4], **Fazle Hussain**[5], **Mauro Ferrari**[1,*], **Xuewu Liu**[1,*], **Seok-Hyun Yun**[2,7,*], and **Paolo Decuzzi**[1,6,♣,*]

[1]Department of Translational Imaging and Department of Nanomedicine, The Methodist Hospital Research Institute, 6670 Bertner Ave, Houston, Texas 77030 – USA

[2]Wellman Center for Photomedicine and Harvard Medical School, Massachusetts General Hospital, 40 Blossom Street, Boston, MA 02114 – USA

[3]Department of Mechanical Engineering, Politecnico di Bari, Via Re David 200, Bari 70125, Italy

[4]Department of Mechanical Engineering and Materials Science, Rice University, 6100 Main St, Houston TX 77005

[5]Department of Mechanical Engineering, University of Houston, Houston, TX 77204-4006

[6]Department of Experimental and Clinical Medicine, University of Magna Graecia, Catanzaro, 88100, Italy

[7]Graduate School of Nano Science and Technology, KAIST, Daejon, Korea

Abstract

Nanoparticles for cancer therapy and imaging are designed to accumulate in the diseased tissue by exploiting the Enhanced Permeability and Retention (EPR) effect. This limits their size to about 100 nm. Here, using intravital microscopy and elemental analysis, we compare the *in vivo* localization of particles with different geometries and demonstrate that plateloid particles preferentially accumulate within the tumor vasculature at unprecedented levels, independent of the EPR effect. In melanoma-bearing mice, 1000×400 nm plateloid particles adhered to the tumor vasculature at about 5% and 10% of the injected dose per gram organ (ID/g) for untargeted and RGD-targeted particles respectively, and exhibited the highest tumor-to-liver accumulation ratios (0.22 and 0.35). Smaller and larger plateloid particles, as well as cylindroid particles, were more extensively sequestered by the liver, spleen and lungs. Plateloid particles appeared well-suited for taking advantage of hydrodynamic forces and interfacial interactions required for efficient tumoritropic accumulation, even without using specific targeting ligands.

♣Corresponding authors. Anne van de Ven, PhD, +1-713 441-7449, avandeven@tmhs.org; Paolo Decuzzi, PhD, +1-713 441-7316, pdecuzzi@tmhs.org.
*These authors shared senior authorship

Keywords

Nanoparticles; Size and shape; Biodistribution; Tumor accumulation; Rational design; Intravital Microscopy

1. Introduction

Many classes of nanoparticles (NPs) have been developed for diverse applications and some have shown potential in the treatment and imaging of diseases [1–4]. Drug encapsulation into NPs can provide significant improvements in pharmacokinetics, toxicity and biodistribution compared to freely administered molecules. Indeed, NP formulations of chemotherapeutic agents have increased by one to two orders of magnitude the peak drug accumulation in tumors[5], however, tumoritropic accumulation rarely exceeds 1% ID/g.

In cancer treatment and imaging, the commonly used strategy for maximizing NP accumulation relies on the enhanced permeation and retention (EPR) effect demonstrated by Maeda and collaborators 25 years ago [6,7]. The tumor vasculature is discontinuous with vessel openings (fenestrations) whose size depends on the tumor type, stage and location [8–10]. Sufficiently small NPs (~100 nm) can passively exit the fenestrated vasculature and reach peak accumulation generally 12 – 24h after injection. Curiously enough, major RES organs, such as the liver and spleen, are characterized by a fenestrated endothelium and utilize this same mechanism to sequester circulating foreign objects. Not surprisingly, a large portion of systemically injected agents and NPs end up accumulating in these RES organs.

Given the NP size limitation introduced by the EPR effect [9–13], efforts to enhance tumoritropic accumulation to-date have mostly focused on the chemical modification of the particle surface. Examples include steric stabilization to increase NP circulation time (*passive targeting*) [5,14], conjugation of ligands for cell-specific recognition (*active targeting*) [15–17], and active NP recruitment using endogenous [18–20] and exogenous [21,22] sources (*cooperative targeting*). Nevertheless, NP accumulation at the intended target is still lower than desired. A judicious choice of the size, shape, and surface combinations, unrelated to the EPR effect, would offer extra degrees of freedom for optimizing tumoritropic accumulation.

Blood is a brilliant example of how different size, shape, and surface combinations can provide circulating objects with diverse functions. For instance, healthy red blood cells (RBCs) can continuously navigate the circulatory system for several weeks while delivering oxygen. The size, shape, and physiochemical properties of the RBC membrane allows these cells to avoid entrapment within the complex microvasculature and, in larger vessels, to repel from the endothelial walls and preferentially stay within the vessel center [23,24]. Conversely, platelets are mostly found in close proximity to the vessel walls, where they can periodically sense for and adhere to sites of vascular injury. This characteristic platelet behavior is ascribed to their small size (3× smaller than RBCs) and quasi-discoidal shape [25,26].

Inspired by these phenomena, we reasoned that plateloid particles – thin disc-like particles – can be used for rapid, efficient, and specific accumulation within the tumor vasculature. Here, we fabricate nanoporous silicon particles with different geometries (size and shape) and surface properties; we monitor in real-time their dynamics using intravital microscopy and quantify, independently, their tissue accumulation by elemental analysis; and we interpret the *in vivo* data, using *in silico* mathematical modeling and *in vitro* adhesion assays, to elucidate the fine mechanisms regulating tumoritropic and RES accumulation.

2. Materials and Methods

2.1 Animal Models

Transgenic Tie2-GFP mice, engineered to express GFP in endothelial cells, were purchased from Jackson Labs (Bar Harbor, ME). The abdominal organs were exposed for intravital imaging via a 1.0 cm midline incision in the abdomen or flank. Melanoma tumors were generated in wild-type C57BL/6J mice (Charles River Laboratories, Wilmington, MA) by a one-time subcutaneous injection of 10^6 mouse B16 cells (ATCC, Manassas, VA). When tumors reached 3–5 mm in diameter were prepared for intravital imaging using a skin-flap procedure. Mice received a onetime injection of fluorescently labeled autologous red blood cells (RBCs) 1–3 days prior to imaging, in order to allow visualization of blood flow dynamics. Briefly, blood collected retro-orbitally was stained with lipophilic carbocyanine DiD (Invitrogen, Carlsbad, CA) at 37°C using the manufacturer's recommended protocol and immediately re-injected behind the contro-lateral eye. Approximately 5% of the total RBCs were labeled per mouse. Thirty minutes after particle injection, mice were sacrificed by gravity perfusion with saline followed by 10% neutral buffered formalin. All intravital animal protocols were reviewed and approved by the IACUC at Massachussetts General Hospital.

2.2 Intravital image acquisition and analysis

Organ-specific accumulation of plateloid silicon particles in vivo was monitored in real-time using a custom, video-rate laser scanning confocal microscope equipped with an x-axis polygon scanner, y-axis galvanometer, 3 lasers (491, 532, and 635 nm), and 3 photomultiplier tubes [34,35] (Supplementary Information). Band pass filters of 30–35 nm width were centered at 425 nm (GFP), 579 nm (particles), and 670 nm (red blood cells). Anesthetized, surgically opened mice were positioned upon the heated stage and injected retro-orbitally with 5×108 particles of a single size (in 50μl PBS). Three-channel images were acquired from a single organ per animal at 30 frames per second from the time of injection using a 40X 0.6 NA dry objective with a pinhole of 100 μm. To minimize local phototoxicity and compensate for tissue heterogeneity, randomly selected non-overlapping regions of interest (ROI, 250×250×6 μm) were imaged continuously for 3 minutes before moving to the next ROI. Animals were imaged for 30 minutes and then sacrificed as described above. A total of 4–8 organs/particle/strain were imaged in real-time. To determine particle accumulation as a function of time, the number of particles per field of view (FOV) was estimated from video stills at 10-second intervals using ImageJ v1.34 (NIH, Bethesda, MD). The 8-bit images were split by color, single pixel noise was removed using a minimum noise filter, and then the total number pixels above a threshold intensity of 50 was divided by the average number pixels per particle. The average number of pixels per particle was experimentally determined for each particle size and confirmed by comparing manual particle counts to automated particle counts. The number of particles per FOV was divided by the optical imaging volume and plotted as a function of time. Representative raw IVM images and quantitative data is shown in Supplementary Figure 9.

2.3 Particle fabrication and conjugation

Porous silicon particles were fabricated by modification of previously described protocols [33], as detailed in the Supplementary Information. Images (Supplementary Figure 8) and characterization data (Supplementary Table 1) are also provided.

2.4 The probability of particle adhesion to the vascular walls

At time $t = 0$, the particle is in close proximity of the vessel wall with all potential ligand-receptor bonds still open (no adhesion). With time, ligands and receptors interact and tend to

form molecular bonds with a probability $p_n(t)$ of having n bonds close at time t governed by the equation [52]

$$\frac{dp_n}{dt} = [A_c m_r - (n-1)]\,[A_c m_l - (n-1)]\,\frac{k_f^{(n)}(t)}{A_c}\,p_{n-1}(t) + (n+1)k_r^{(n+1)}(t)\,p_{n+1}(t) - \left[(A_c m_r - n)(A_c m_l - n)\frac{k_f^{(n+1)}(t)}{A_c} + n k_r^{(n)}(t)\right] p_n(t) \quad (1)$$

where $k_f^{(n)}(t)$ and $k_r^{(n)}(t)$ are the forward (association) and reverse (dissociation) rates at time t for n close bonds. A_c is the area of adhesion which is given by πd^2 for a plateloid particle with diameter d). Assuming for simplicity a uniform distribution of the hydrodynamic dislodging forces over the n molecular bonds at each time t, the reactions rates take the explicit forms

$$k_r^{(n)}(t) = k_{ro}\exp\left[\frac{\chi}{k_B T}\frac{F_{tot}(t)}{m_b A_c}\right] \qquad k_f^{(n)}(t) = k_{fo}\left[1 + \frac{\chi}{n k_B T}\frac{F_{tot}(t)}{m_b A_c}\right]^{-1} \quad (2)$$

where χ (= 0.1 nm) is the characteristic bond length, and $k_B T$ is the Boltzmann thermal energy (= 4.14×10^{-21} J). k_{fo} and k_{ro} are the forward and reverse rates at zero mechanical load, and their ratio k_{ao} (= k_{fo}/k_{ro}) is the ligand-receptor affinity at zero mechanical load. The ligand-receptor bond density m_b is equal to the minimum value between m_r and m_l. Equation (2) is then solved numerically for different values of n imposing the initial conditions ($p_n(0) = 0$ for $n > 1$; and $p_o(0) = 1$) and the closure condition (at each time t). The probability of adhesion P_a is defined as the probability of having at least one ligand-receptor bond close and is easily estimated as $P_a(t) = 1 - p_o(t)$.

The generalized force F exerted over the adhering plateloid particle are estimated, following previous work [53], as $F = \pi A \mu S a^2$, where S is the wall shear rate, μ is the plasma viscosity (2.5×10^{-3} Pa×sec), and the coefficient A depends on the aspect ratio b/a, which is ~ 0.35 in the present analysis.

3. Results and Discussion

3.1 Nanoporous silicon plateloids and cylindroids

Precise control over multiple scales of the NP size, shape, and surface properties can be reliably achieved with few technologies [27–30]. Nanoporous silicon particles were chosen for these studies due to their documented advantages in the treatment and imaging of tumors [31–35]. Particles of different geometries were fabricated using two consecutive steps: formation of a porous silicon film and micropatterning. The particle porosity and pore size were tailored by electrochemical etching, controlling parameters such as silicon doping, etching current, and HF concentration; while the particle size was precisely defined by photolithography. Since the pore structure and particle geometry are independently controlled, a wide range of size, shape and pore morphologies can be reliably achieved with such an approach [36]. Three sizes of plateloid particles with similar aspect ratios were fabricated: 600×200 nm, 1000×400 nm, and 1800×600 nm. Two sizes of cylindroid particles were fabricated: 1500×200 nm and 1800×400 nm, which exhibit a volume equivalent to that of the two smaller plateloid particles. Figure 1a shows SEM images of plateloid and cylindroid particles before and after release from the original silicon wafer.

Particles of plateloid and cylindroid shape are expected to exhibit fairly complex dynamics under flow and will tend to drift laterally across the stream lines in a periodic manner (Figure 1b – Margination inset). Particle interaction with the vessel walls is a critical step for the recognition of the diseased vasculature. *In silico* mathematical models have shown that lateral drifting diminishes as the NP size decreases, becoming irrelevant for particles of ~ 100 nm or less [37]. Also, moving from spherical to anisometric particles increases lateral drifting, as well as the probability of firm vascular adhesion because of the larger surface area exposed to the endothelial wall [38] (Figure 1b – Adhesion inset). Sub-micrometer and micrometer anisometric particles offer the further advantage of a high cargo capacity, allowing for the localized release of therapeutic and imaging agents at the site of vascular adhesion (Figure 1b – Release inset).

The nanoporous silicon particles were labeled with fluorescent dye molecules for optical tracking within the blood flow. Their dynamics was monitored in live mice following systemic injection using high-resolution, video-rate intravital microscopy (IVM) [39,40]. Figure 1c captures some of the distinctive features exhibited by individual particles within the microvasculature, including differential transport velocities and adhesion to the vessel walls.

3.2 Particle localization at the organ scale

To evaluate the importance of particle geometry (size and shape) for organ accumulation, the biodistribution of individual particles was examined (Figure 2). Figure 2a shows representative images of particle accumulation in different organs, collected *in vivo* one hour after injection. Videos of particle accumulation and additional images are provided in the Supplementary Information (Supplementary Figures S1 and S2, and Supplementary Movies 1 and 2). This IVM technique was used, for the first time, to quantify the time-dependent accumulation of the particles in live mice (Figure 2a). Figure 2b shows the accumulation of 600×200 and 1000×400 nm plateloid particles in three different organs of wild-type, melanoma-bearing mice. Unlike EPR-based delivery strategies, the accumulation of these particles was most rapid for the first 5 – 10 min after injection, and then began to level off. Note that, in the liver and spleen, 600×200 plateloid particles accumulated faster and in greater numbers (~ 3×) than the 1000×400 nm. This trend was reversed in tumor tissue (~ 1/4×). The cumulative particle uptake measured by IVM is shown in Figure 3a, where the effect of particle geometry can be readily appreciated.

Using ICP-AES, the total number of accumulated particles was independently quantified in whole organs after animal sacrifice. The particle biodistribution, expressed in terms of percentage of the injected dose normalized by the organ weight, shows that geometry (size and shape) plays a significant role in the ability of NPs to preferentially accumulate in different tissues (Figure 3b). In liver and spleen, 600×200 nm plateloid particles display the highest accumulation efficiency. In contrast, cylindroid particles accumulate at much higher levels than plateloid particles in the lungs. Most interestingly, in the tumor, 1000×400 nm plateloid particles demonstrate the highest accumulation efficiency of all particles examined (5% ID/g tumor). The trends observed in the IVM data (Figure 3a) and ICP-AES data (Figure 3b, Supplementary Figure 3) are in good qualitative agreement.

Several of the animals receiving cylindroid particles died spontaneously between 30 – 60 min after injection, showing signs of labored breathing before death and gross signs of lung emboli upon necropsy. It is possible that these rigid cylindroid particles have a similar capacity for causing lung emboli as the so called ‘ugly’ nanotubes [41]. Shorter cylindroid particles may provide different biodistributions, but also much lower payloads due to their smaller volume. Since no complications were observed with plateloid particles, these were used for assessing the importance of molecular targeting in tumors.

Fluorescently tagged plateloid particles were derivatized with a cyclic arginine-glycine-aspargine (RGD-4C) peptide via a short PEG linker to produce particles of identical size, shape, and surface charge but with a high affinity for the $\alpha_v\beta_3$ integrins overexpressed on the tumor endothelium. Figure 4a shows the time-dependent accumulation of targeted and untargeted plateloid particles in tumors, measured with IVM. The cumulative particle uptake was independently quantified using ICP-AES (Figure 4b). For untargeted particles, the level of accumulation varied from 1.2% (600×200nm) to 5.1% (1000×400 nm) to 3.2% ID/g (1800×600 nm). The use of RGD-4C moieties increases tumor-specific accumulation, presenting as 4.5% (600×200 nm), 8.1% (1000×400 nm), and 6.5% ID/g (1800×600 nm) respectively. Interestingly, a maximum appears for the 1000×400 nm particles, regardless of the surface properties. The enhancement in particle accumulation with RGD-4C addition was size-dependent, with the smallest particles showing the greatest enhancement (300% versus 50% for 600×200 and 1000×400 nm particles respectively). The 1000×400 nm particles exhibit the highest tumor-to-liver accumulation ratio, being equal to about 0.22 and 0.35 for untargeted and targeted plateloids respectively. This unprecedented, rapid tumoritropic accumulation was achieved using particles significantly larger than known tumor fenestration sizes.

3.3 Particle localization at the sub-organ scale

In tumors, the 1000×400 nm particles were observed to be confined within the blood vessels using both IVM and SEM imaging (Figure 4c, top). Particle adhesion occurred in both fenestrated and non-fenestrated regions of the tumor vasculature (Supplementary Figure 4). Differently, some 600×200 nm particles (5–10% untargeted, <1% targeted) were seen outside the vascular compartment (Figure 4c, bottom). This is likely associated with the highly fenestrated vessels and poorly organized melanoma tissue through which the smaller plateloid particles may diffuse (Figure 4d).

For the major RES organs, particle association with cells of the immune system was studied using IVM, immunocytochemistry, and histological analysis (Figures 5 and Supplementary Figure 5, 6). Immunocytochemistry images showed that >80% of plateloid and cylindroid particles in the liver were associated with Kupffer cells (Figures 5a,b and Supplementary Figure 5). In the spleen, a similar trend was observed for the two larger plateloid particles (>70%), whereas only 50% of the 600 nm particles associated with the splenic macrophages (Figures 5a,b). This difference may be ascribed to the smaller size of the 600×200 nm particles, which are more prone to geometrical trapping in the splenic fenestrations, as confirmed by histological analysis (Figure 5c). Like the 600×200 nm plateloid particles, the 1500×200 nm cylindroid particles displayed an increased propensity to accumulate at the margins of the white pulp, as compared to their thicker counterparts which remained uniformly distributed in the red pulp (Supplementary Figure 5b). Figures 5d,e show SEM sections of the liver vasculature capturing different stages of the cell-particle interaction *in vivo*: first circulating particles firmly adhere to the surface of Kupffer cells (Figure 5d), then pseudopodia protrude out of the cell membrane and start to gently embrace the particles (Figure 5d), and eventually particles are pulled inside the cell (Figure 5e). In the tumor and other tissues, the percentage of particles associated with macrophages is negligibly small (Figure 5a, Supplementary Figure 5a).

3.4 Mechanisms regulating preferential particle accumulation

Vascular adhesion and internalization by immune cells lining the vessel walls, such as the Kuppfer cells in the liver and the splenic macrophages, are finely regulated by the interplay between hydrodynamic forces and interfacial interactions. The latter primarily originate from the binding of receptors, expressed over the cell membrane with a density m_r, to ligands, coating the particles surface with a density m_l [38]. Colloidal forces may also arise

at the particle-cell interface but are generally much weaker than molecular interactions, especially in plasma [42]. Particle surfaces can be functionalized with ligands during synthesis or opsinized upon contact with the blood stream [43]. Nanoporous silicon particles are coated to different extents by plasma molecules which act as ligands for the CR1 and Fc receptors expressed by cells of the immune system [44].

Following the formulation presented in the Materials and Methods, a probability of particle adhesion P_a to the blood vessels can be estimated as a function of design parameters (geometry, ligand density m_l, ligand-receptor affinity k_a) and biophysical conditions at the adhesion site (wall shear rate S, receptor density m_r). Figure 6a shows the variation of P_a for plateloid particles with a diameter d and for different values of the shear rate S, having fixed all the other parameters. For wall shear rates typically found in the leaky tumor vessels (low S) [8], the P_a curves exhibit a maximum at about 1000 nm. Moving from pathological to normal vessels ($S > 500$ sec^{-1}), the maximum in strength of adhesion occurs at smaller d (Supplementary Information). The existence of an optimal geometry (size and shape) maximizing vascular adhesion was previously conjectured [37] and explained as: for small particles, the interfacial area offered to the vessel walls for developing stable and strong adhesive forces is insufficient (*area limited regime*); on the other hand, for large particles, the hydrodynamic dislodging forces are excessively large to be balanced by interfacial adhesion interactions (*force limited regime*). This fine balance was recently observed experimentally for spherical beads [45] and, here, confirmed for plateloid particles (Figure 6b).

Using a parallel plate flow chamber, the adhesive strength of untargeted plateloid particles was quantified as a function of diameter d and wall shear rate S. As shown in Figure 6b, the 1000 nm particles adhere more avidly at all S, followed by the 1800 nm and by the 600 nm particles. As S increases, the overall number of adhering particles reduces. The strong agreement between the tumor accumulation data (Figure 4b), theoretical predictions (Figure 6a), and *in vitro* experiments (Figure 6b) suggests that vascular adhesion may be dominant mechanism for their tumor accumulation. This is also supported by the IVM images presented in Figure 4c.

The effect of the receptor density m_r and ligand-receptor affinity k_a on the probability of adhesion P_a was also estimated and shown in Figure 6c,d. Both parameters, although independent, characterize the specificity of molecular targeting. Consequently, the two plots in Figure 6c,d are qualitatively similar and manifest the growth in adhesive strength with the improvement in molecular specificity (i.e. larger m_r and k_a). Indeed, this is true under the idealized conditions of the *in silico* modeling and *in vitro* experiments, but it is also in agreement with the accumulation data presented for the RGD-4C modified particles (Figure 4b). Again, the optimal diameter d is not significantly affected by the particles surface properties (targeted and untargeted), unless extremely large m_r and k_a are considered (Supplementary Information).

Particles in the liver and the spleen, unlike tumors, are taken up by immune cells lining the blood vessels in these organs (Figure 5). Therefore, adhesion and subsequent cell internalization should be considered in series to correctly interpret the quantitative data of Figure 3. In this case, particle adhesion is mediated by the CR1 and Fc receptors, which are highly expressed on the membrane of phagocytic cells ($m_r = 10^3$ and 10^5 #/μm^2, depending on the stimulation state [46]). Under these conditions, P_a is extremely large regardless of the particle size. On the other hand, the internalization rate is affected by the particle size. In agreement with data in the literature [47], J774.1 macrophages were found *in vitro* to internalize 600×200 nm particles faster than the 1000×400 nm (Supplementary Figure 7). As a consequence, the probability of internalization – probability of adhesion × rate of

internalization – is greater for 600×200nm particles compared to larger particles. This would explain the higher accumulation observed for the smaller plateloid particles in the liver and spleen (Figure 2a and 3).

4. Conclusions

In current practice, systemically injected NPs rely on the EPR effect to preferentially accumulate within tumors. Using this delivery strategy, few NPs have achieved tumor accumulation greater than 1% ID/g. Here we demonstrate rapid (< 1h) and unprecedented (~ 10% ID/g) accumulation of 1000×400 nm plateloid particles in the tumor vasculature. The use of an EPR-independent delivery strategy allowed additional degrees of freedom over traditional tumoritropic accumulation schemes. Particle size, shape, and surface properties were all found to play an important role. In particular, 1000×400 nm plateloid particles appeared well-suited for taking advantage of hydrodynamic forces and interfacial interactions required for efficient tumoritropic accumulation, even without the use of specific targeting ligands. Smaller plateloid particles accumulated more extensively in the liver and spleen, whereas larger plateloid particles deposited more in the lungs. Cylindroid particles exhibited a significantly lower tumor-to-liver accumulation ratio.

Plateloid particles designed to recognize and adhere to diseased vessels may be employed to deliver anti-angiogenic agents directly to endothelial cells [48], thermally ablate blood vessels supplying the tumor mass [49], or to locally deploy cargos (drug molecules, contrast agents, NPs, etc) to tumors characterized by small fenestrations. Furthermore, they may exploit the huge diversity of biomarkers that differentiate normal from abnormal endothelia for potentially treating and imaging a variety of pathologies, including cardiovascular, hemorrhagic, and neurodegenerative diseases [50,51].

Collectively, these results demonstrate that plateloid particles of the proper size, shape, and surface properties significantly enhance tumoritropic particle accumulation. Without relying on the EPR effect, they may offer notable therapeutic and imaging potential for a variety of diseases.

Supplementary Material

Refer to Web version on PubMed Central for supplementary material.

Acknowledgments

This work was supported by Telemedicine and Advanced Technology Research Center (TATRC)-United States Army Medical Research Acquisition Activity (USAMRAA) through the pre-centre grant W81XWH-09-2-0139 of the Alliance for Nano Health. This work was also partially supported through grants from the National Institutes of Health (USA) (NIH) U54CA143837 and U54CA151668, and the Department of Defense (DoD) grant W81XWH-09-1-0212. The authors would like to thank Mr. Matthew Landry for helping with the graphical work, Mr. Aaron Mack for advice on particle conjugation and ICP-AES protocols, as well as Dr. W.M. Steve Lee and Dr. Jinwoo Choi for helping with animal preparations. PD would like to thank the President and staff at the University of Magna Graecia – Italy for their support.

References

1. Allen TM, Cullis PR. Drug delivery systems: entering the mainstream. Science. 2004; 19:1818–1822. [PubMed: 15031496]
2. Huang HC, Barua S, Sharma G, Dey SK, Rege K. Inorganic nanoparticles for cancer imaging and therapy. J Control Release. 2011 Jul 18. [e-published ahead of print].
3. Ferrari M. Cancer nanotechnology: opportunities and challenges. Nature Reviews Cancer. 2005; 5:161–171.

4. Peer D, Karp JM, Hong S, Farokhzad OC, Margalit R, Langer R. Nanocarriers as an emerging platform for cancer therapy. Nature Nanotechnology. 2007; 2:751–760.
5. Drummond DC, Meyer O, Hong K, Kirpotin DB, Papahadjopoulos D. Optimizing liposomes for delivery of chemotherapeutic agents to solid tumors. Pharmacol Rev. 1999; 51:691–743. [PubMed: 10581328]
6. Matsumura Y, Maeda H. A new concept for macromolecular therapeutics in cancer chemotherapy: Mechanism of tumoritropic accumulation of proteins and the antitumor agent smancs. Cancer Res. 1986; 46:6387–6392. [PubMed: 2946403]
7. Maeda H, Wu J, Sawa T, Matsumura Y, Hori K. Tumor vascular permeability and the EPR effect in macromolecular therapeutics: a review. J Control Release. 2000; 65:271–84. [PubMed: 10699287]
8. Jain RK, Stylianopoulos T. Delivering nanomedicine to solid tumors. Nat Rev Clin Oncol. 2010; 7:653–64. [PubMed: 20838415]
9. Yuan F, Leunig M, Huang SK, Berk DA, Papahadjopoulos D, Jain RK. Microvascular permeability and interstitial penetration of sterically stabilized (stealth) liposomes in a human tumor xenograft. Cancer Res. 1994; 54:3352–3356. [PubMed: 8012948]
10. Hobbs SK, Monsky WL, Yuan F, Roberts WG, Griffith L, Torchilin VP, Jain RK. Regulation of transport pathways in tumor vessels: role of tumor type and microenvironment. Proc Natl Acad Sci USA. 1998; 95:4607–12. [PubMed: 9539785]
11. Campbell RB, Fukumura D, Brown EB, Mazzola LM, Izumi Y, Jain RK, Torchilin VP, Munn LL. Cationic charge determines the distribution of liposomes between the vascular and extravascular compartments of tumors. Cancer Res. 2002; 62:6831–6836. [PubMed: 12460895]
12. Dellian M, Yuan F, Trubetskoy S, Torchilin P, Jain RK. Vascular permeability in a human tumour xenograft: molecular charge dependence. Br J Cancer. 2000; 82:1513–1518. [PubMed: 10789717]
13. Stroh M, Zimmer JP, Duda DG, Levchenko TS, Cohen KS, Brown EB, Scadden DT, Torchilin VP, Bawendi MG, Fukumura D, Jain RK. Quantum dots spectrally distinguish multiple species within the tumor milieu in vivo. Nat Med. 2005; 11:678–82. [PubMed: 15880117]
14. Moghimi SM, Hunter AC, Murray JC. Nanomedicine: current status and future prospects. FASEB J. 2005; 19:311–30. [PubMed: 15746175]
15. Elbayoumi TA, Torchilin VP. Enhanced accumulation of long-circulating liposomes modified with the nucleosome-specific monoclonal antibody 2C5 in various tumours in mice: gamma-imaging studies. Eur J Nucl Med Mol Imaging. 2006; 33:1196–205. [PubMed: 16763815]
16. Cheng J, Teply BA, Sherifi I, Sung J, Luther G, Gu FX, Levy-Nissenbaum E, Radovic-Moreno AF, Langer R, Farokhzad OC. Formulation of functionalized PLGA-PEG nanoparticles for in vivo targeted drug delivery. Biomaterials. 2007; 28:869–76. [PubMed: 17055572]
17. Wang MD, Shin DM, Simons JW, Nie S. Nanotechnology for targeted cancer therapy. Expert Rev Anticancer Ther. 2007; 7:833–837. [PubMed: 17555393]
18. Lu W, Xiong C, Zhang G, Huang Q, Zhang R, Zhang JZ, Li C. Targeted photothermal ablation of murine melanomas with melanocyte-stimulating hormone analog-conjugated hollow gold nanospheres. Clin Cancer Res. 2009; 15:876–86. [PubMed: 19188158]
19. Park JH, von Maltzahn G, Xu MJ, Fogal V, Kotamraju VR, Ruoslahti E, Bhatia SN, Sailor MJ. Cooperative nanomaterial system to sensitize, target, and treat tumors. Proc Natl Acad Sci USA. 2010; 107:981–6. [PubMed: 20080556]
20. von Maltzahn G, Park JH, Lin KY, Singh N, Schwöppe C, Mesters R, Berdel WE, Ruoslahti E, Sailor MJ, Bhatia SN. Nanoparticles that communicate in vivo to amplify tumour targeting. Nat Mater. 2011; 10:545–52. [PubMed: 21685903]
21. Chertok B, David AE, Huang Y, Yang VC. Glioma selectivity of magnetically targeted nanoparticles: a role of abnormal tumor hydrodynamics. J Control Release. 2007; 122:315–23. [PubMed: 17628157]
22. Liu HL, Hua MY, Yang HW, Huang CY, Chu PC, Wu JS, Tseng IC, Wang JJ, Yen TC, Chen PY, Wei KC. Magnetic resonance monitoring of focused ultrasound/magnetic nanoparticle targeting delivery of therapeutic agents to the brain. Proc Natl Acad Sci USA. 2010; 107:15205–10. [PubMed: 20696897]
23. Kim S, Ong PK, Yalcin O, Intaglietta M, Johnson PC. The cell-free layer in microvascular blood flow. Biorheology. 2009; 46:181–9. [PubMed: 19581726]

24. Lipowsky HH. Microvascular rheology and hemodynamics. Microcirculation. 2005; 12:5–15. [PubMed: 15804970]
25. Yeh C, Eckstein EC. Transient lateral transport of platelet-sized particles in flowing blood suspensions. Biophys J. 1994; 66:1706–16. [PubMed: 8061219]
26. Saadatmand M, Ishikawa T, Matsuki N, Jafar Abdekhodaie M, Imai Y, Ueno H, Yamaguchi T. Fluid particle diffusion through high-hematocrit blood flow within a capillary tube. J Biomech. 2011; 44:170–5. [PubMed: 20887991]
27. Cohen MH, Melnik K, Boiarski AA, Ferrari M, Martin FJ. Microfabrication of Silicon-Based Nanoporous Particulates for Medical Applications. Biomedical Microdevices. 2003; 5:253–259.
28. Gratton SE, Pohlhaus PD, Lee J, Guo J, Cho MJ, Desimone JM. Nanofabricated particles for engineered drug therapies: a preliminary biodistribution study of PRINT nanoparticles. J Control Release. 2007; 21:10–18. [PubMed: 17643544]
29. Champion JA, Katare YK, Mitragotri S. Making polymeric micro- and nanoparticles of complex shapes. Proc Natl Acad Sci USA. 2007; 104:11901–4. [PubMed: 17620615]
30. Acharya G, Shin CS, McDermott M, Mishra H, Park H, Kwon IC, Park K. The hydrogel template method for fabrication of homogeneous nano/microparticles. J Control Release. 2010; 141:314–9. [PubMed: 19822178]
31. Tasciotti E, Liu X, Bhavane R, Plant K, Leonard AD, Price BK, Cheng MM, Decuzzi P, Tour JM, Robertson F, Ferrari M. Mesoporous silicon particles as a multistage delivery system for imaging and therapeutic applications. Nat Nanotechnol. 2008; 3:151–7. [PubMed: 18654487]
32. Park JH, Gu L, von Maltzahn G, Ruoslahti E, Bhatia SN, Sailor MJ. Biodegradable luminescent porous silicon nanoparticles for in vivo applications. Nat Mater. 2009; 8:331–6. [PubMed: 19234444]
33. Meng H, Liong M, Xia T, Li Z, Ji Z, Zink JI, Nel AE. Engineered design of mesoporous silica nanoparticles to deliver doxorubicin and P-glycoprotein siRNA to overcome drug resistance in a cancer cell line. ACS Nano. 2010; 4:4539–50. [PubMed: 20731437]
34. Ananta JS, Godin B, Sethi R, Moriggi L, Liu X, Serda RE, Krishnamurthy R, Muthupillai R, Bolskar RD, Helm L, Ferrari M, Wilson LJ, Decuzzi P. Geometrical confinement of gadolinium-based contrast agents in nanoporous particles enhances T1 contrast. Nat Nanotechnol. 2010; 5:815–821. [PubMed: 20972435]
35. Tanaka T, Mangala LS, Vivas-Mejia PE, Nieves-Alicea R, Mann AP, Mora E, Han HD, Shahzad MM, Liu X, Bhavane R, Gu J, Fakhoury JR, Chiappini C, Lu C, Matsuo K, Godin B, Stone RL, Nick AM, Lopez-Berestein G, Sood AK, Ferrari M. Sustained small interfering RNA delivery by mesoporous silicon particles. Cancer Res. 2010; 70:3687–96. [PubMed: 20430760]
36. Chiappini C, Tasciotti E, Fakhoury JR, Fine D, Pullan L, Wang YC, Fu L, Liu X, Ferrari M. Tailored porous silicon microparticles: fabrication and properties. Chemphyschem. 2010; 11:1029–1035. [PubMed: 20162656]
37. Lee SY, Ferrari M, Decuzzi P. Shaping nano-/micro-particles for enhanced vascular interaction in laminar flows. Nanotechnology. 2009; 20:495101. [PubMed: 19904027]
38. Decuzzi P, Ferrari M. The adhesive strength of non-spherical particles mediated by specific interactions. Biomaterials. 2006; 27:5307–14. [PubMed: 16797691]
39. Kim P, Puoris'haag M, Cote D, Lin CP, Yun SH. In vivo confocal and multiphoton microendoscopy. Journal of Biomedical Optics. 2008; 13:010501. [PubMed: 18315346]
40. Fan Z, Spencer J, Yan Lu Y, Pitsillides CM, Singh G, Kim P, Yun SH, Strom TB, Lin CP, Koulmanda M. In vivo tracking of color coded effector, natural and induced regulatory T cells in allograft response. Nature Medicine. 2010; 16:718–722.
41. Kostarelos K, Bianco A, Prato M. Promises, facts and challenges for carbon nanotubes in imaging and therapeutics. Nat Nanotechno. 2009; l4:627–633.
42. Israelachvili, JN. With Applications to Colloidal and Biological Systems. 2. Academic Press; 1992. Intermolecular and Surface Forces.
43. Owens DE III, Peppas NA. Opsonization, biodistribution, and pharmacokinetics of polymeric nanoparticles. Int J Pharm. 2006; 307:93–102. [PubMed: 16303268]
44. Serda RE, Blanco E, Mack A, Stafford SJ, Amra S, Li Q, van de Ven A, Tanaka T, Torchilin VP, Wiktorowicz JE, Ferrari M. Proteomic analysis of serum opsonins impacting biodistribution and

cellular association of porous silicon microparticles. Mol Imaging. 2011; 10:43–55. [PubMed: 21303614]

45. Boso DP, Lee SY, Ferrari M, Schrefler BA, Decuzzi P. Optimizing Particle Size for Targeting the Diseased Microvasculature: from Experiments to Artificial Neural Networks. Int J of Nanomedicine. 2011; 6:1517–1526. [PubMed: 21845041]
46. van Es LA, Daha MR. Factors influencing the endocytosis of immune complexes. Adv Nephrol Necker Hosp. 1984; 13:341–67. [PubMed: 6236677]
47. Sharma G, Valenta DT, Altman Y, Harvey S, Xie H, Mitragotri S, Smith JW. Polymer particle shape independently influences binding and internalization by macrophages. J Control Release. 2010; 147:408–12. [PubMed: 20691741]
48. Sengupta S, Eavarone D, Capila I, Zhao GL, Watson N, Kiziltepe T, et al. Temporal targeting of tumour cells and neovasculature with a nanoscale delivery system. Nature. 2005; 436:568–572. [PubMed: 16049491]
49. West JL, Halas NJ. Engineered nanomaterials for biophotonics applications: improving sensing, imaging, and therapeutics. Annu Rev Biomed Eng. 2003; 5:285–292. [PubMed: 14527314]
50. Pasqualini R, Arap W, McDonald DM. Probing the structural and molecular diversity of tumor vasculature. Trends Mol Med. 2002; 8:563–571. [PubMed: 12470989]
51. Lee GY, Kim JH, Oh GT, Lee BH, Kwon IC, Kim IS. Molecular targeting of atherosclerotic plaques by a stabilin-2-specific peptide ligand. J Control Release. 2011 Jul 14. [e-published ahead of print].
52. Piper JW, Swerlick RA, Zhu C. Determining Force Dependence of Two-Dimensional Receptor-Ligand Binding Affinity by Centrifugation. Biophysical Journal. 1998; 74:492–513. [PubMed: 9449350]
53. Pozrikidis C. Shear flow over a protuberance on a plane wall. Journal of Engineering Mathematics. 1995; 31:29–42.

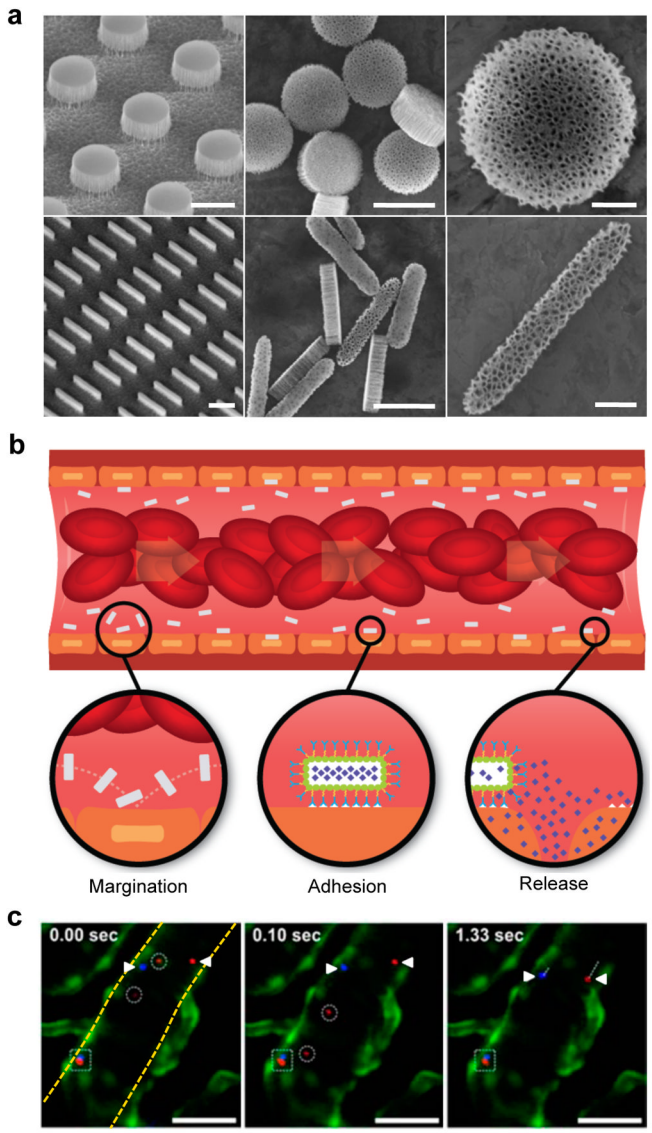

Figure 1. Rationally designed nanoporous silicon particles

a, SEM images of nanoporous plateloid (1000×400 nm) and cylindroid (1500×200 nm) silicon particles micropatterned from a porous film before (left) and after release (middle, right) (scale bars, 1.0, 1.0, and 0.25 μm). b, Longitudinal cross-section illustration of a blood vessel containing circulating red blood cells and silicon particles traveling through and adhering to the walls. Margination inset: The lateral drifting of anisometric particles promotes periodic interaction with the vessel walls; Adhesion inset: The large surface area of anisometric particles favors specific and non-specific interactions with receptors on the endothelial surface; Release inset: The release of cargo by adherent particles facilitates localized delivery into the underlying tissue. c, Intravital microscopy images showing time-dependent trajectories of individual 600×200 nm (red) and 1000×400 nm (blue) plateloid silicon particles in the ear venule of a Tie-2 GFP+ mouse. The triangles indicate relatively slow moving particles (μm/sec), the circles indicate fast moving particles (μm/msec), and the square indicates particles adhered to the vessel wall. Endothelial cells are colored green, vessel walls are demarcated in yellow (scale bar, 50 μm).

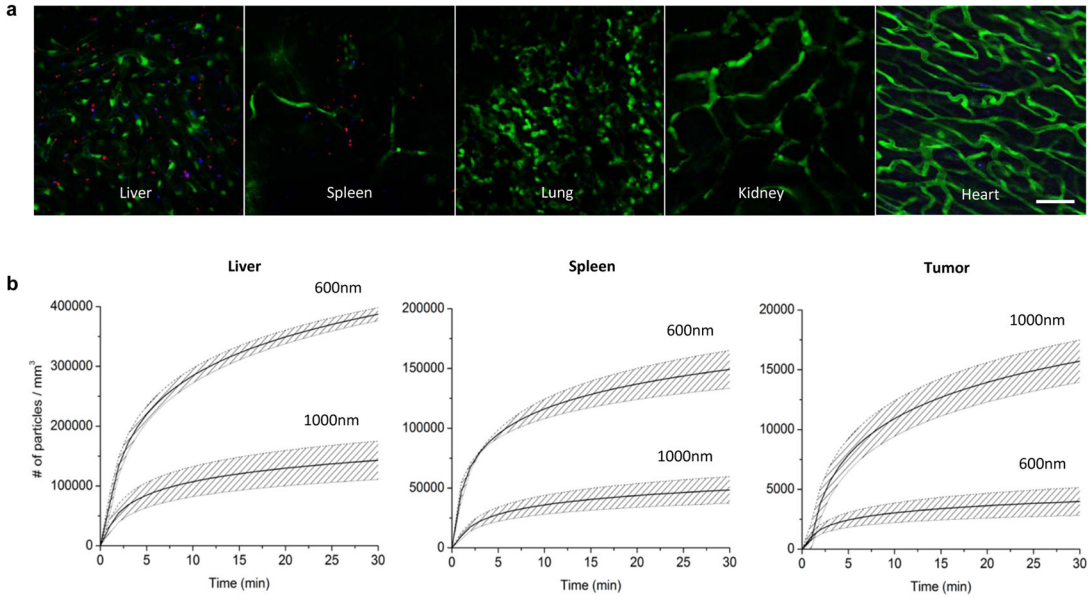

Figure 2. Biodistribution of plateloid particles in live mice

a, Distribution of 600×200 nm (red) and 1000×400 nm (blue) plateloid silicon particles in different organs of Tie2-GFP+ mice 1h after simultaneous systemic injection (scale bar, 50 μm). b, Time-dependent accumulation of plateloid particles (injected independently) in two major RES organs – the liver and the spleen – and in the tumor tissue of melanoma-bearing mice, measured using intravital microscopy. Data is plotted as a mean curve ± 1 SD (n=4 animals).

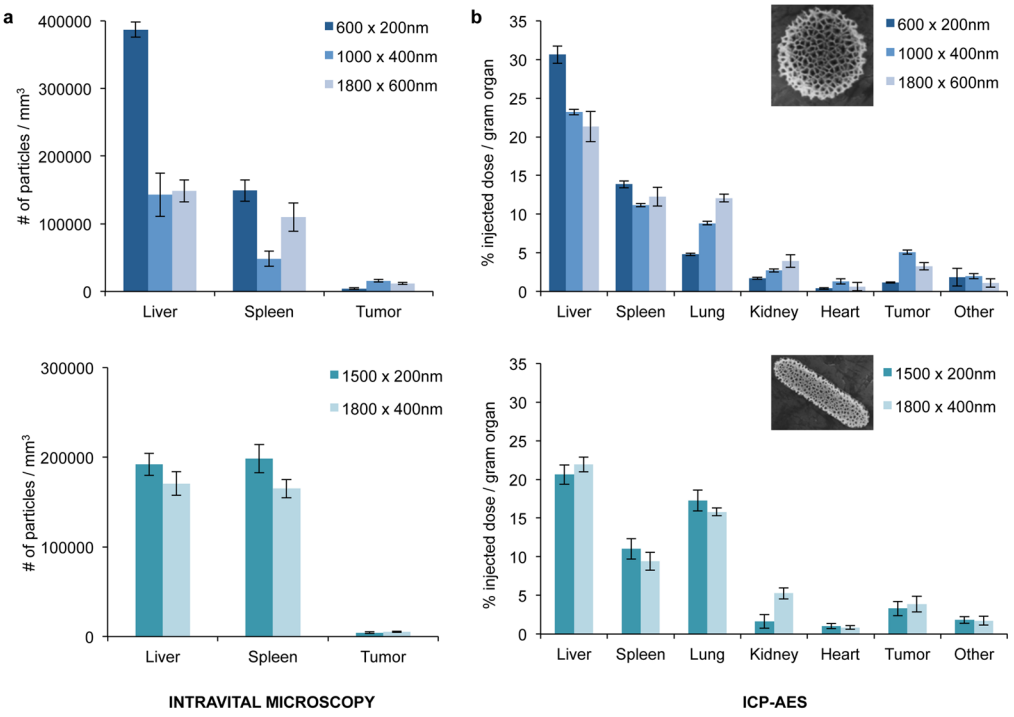

Figure 3. Cumulative particle localization at the organ level: The effect of particle geometry

a, Intravital data on the cumulative uptake of plateloid (top) and cylindroid (bottom) particles 30 minutes after injection. b, ICP-AES data on the cumulative uptake of plateloid (top) and cylindroid (bottom) particles expressed as a percentage of the injected dose normalized by the tissue mass. Similar trends are observed with the two independent techniques.

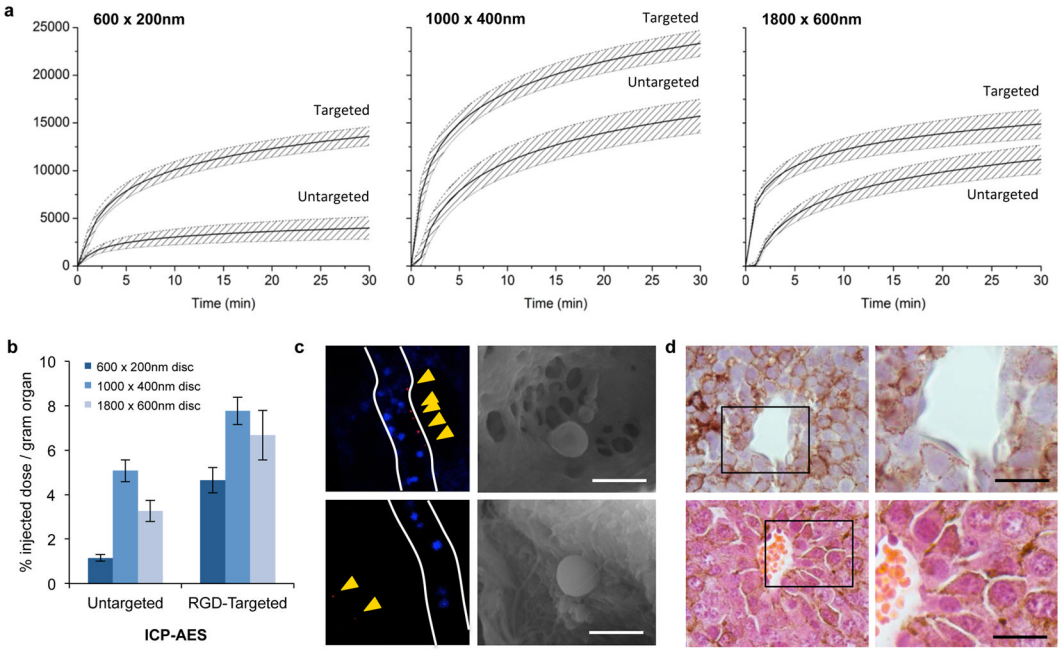

Figure 4. Accumulation of untargeted and RGD-targeted plateloid particles in melanoma tumors

a, Intravital microscopy data on the time-dependent accumulation of 600×200 nm (left), 1000×400 nm (center), and 1800×600 nm (right) plateloid particles. b, ICP-AES data on the cumulative particle uptake expressed as percentage of the injected dose normalized by the tumor mass. c, Stills extracted from intravital videos reveal that 1000×400 nm particles accumulate within the tumor vasculature (top left), whereas some 600×200 nm particles extravasate out of the vasculature (bottom left). The SEM sections clearly show the fenestrations in the tumor vasculature and their size relative to the plateloid particles (scale bar, 1.0 μm). d, Representative histological images of the tissue surrounding the tumor vasculature. The vessel wall is poorly organized with gaps between endothelial cells (top). The tumor cells are poorly packed, resulting in gaps between cells (bottom) (scale bar, 1.0 μm).

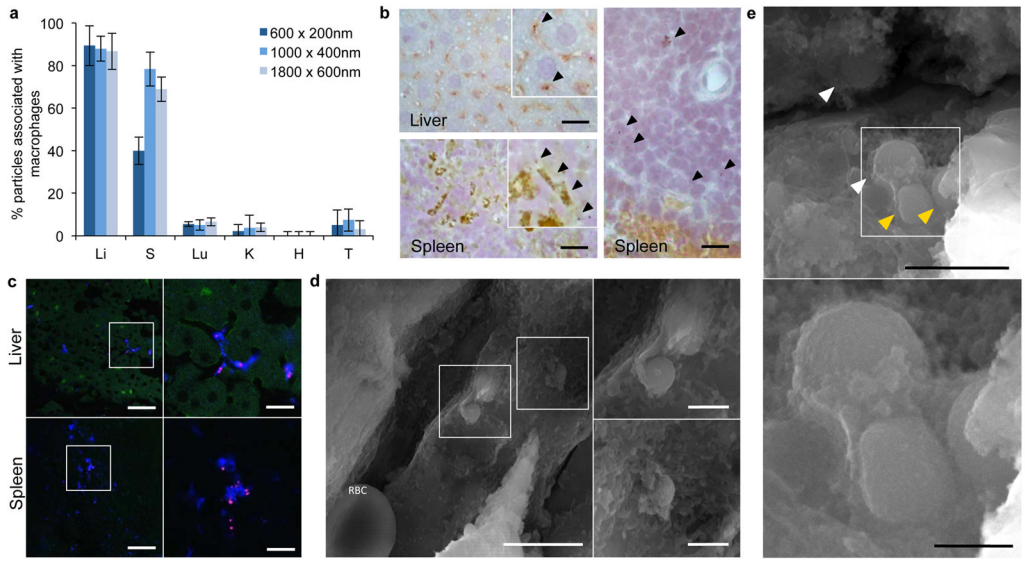

Figure 5. Sequestration of plateloid particles by immune cells

a, Percentage of particles co-localized with immune cells in different organs, measured using immunocytochemistry of fixed tissue cross-sections (Li: Liver; S: Spleen; Lu: Lungs; K: Kidneys; H: Heart and T: Tumor). b, Confocal fluorescence images of 1000×400 nm particles (red) co-localizing with CD204+ macrophages (blue) in fixed liver and spleen tissue. c, IHC images of 1000×400 nm (left) and 600×200 nm (right) particles in the liver and spleen. CD204+ macrophages are stained in brown. d, SEM images of 1000×400 nm particles in the liver vasculature being internalized by a Kupffer cell. A red blood cell (RBC) is visible at the bottom left of the larger image (scale bars, 5.0 and 1.0 μm). e, SEM images of 600×200 nm particles in the liver vasculature. The yellow arrows indicate particles that have been internalized; the white arrows indicate particles undergoing internalization (scale bars, 2.0 and 0.5 μm).

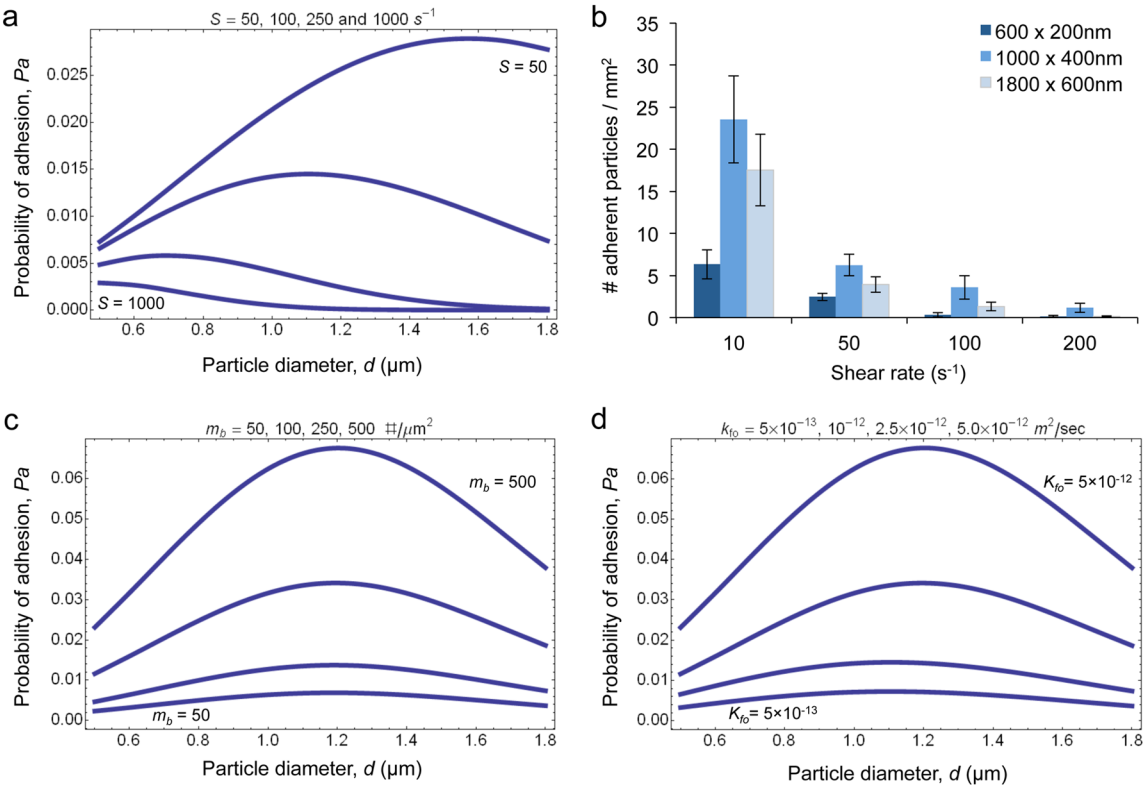

Figure 6. Adhesion of plateloid particles

a, The probability of adhesion (P_a) for plateloid particles is shown as a function of the diameter d and for different shear rates S ($m_r = 10^{+2}$ #/μm^2; $m_l = 10^{+4}$ #/μm^2, $k_{ao} = 10^{-9}$ μm^2); b, Number of plateloid particles adhering per unit area to the bottom of a parallel plate flow chamber, under different hydrodynamic conditions; c, P_a as a function of the particle diameter d and for different receptor densities m_b ($S = 100$ sec^{-1} ; $m_l = 10^{+4}$ #/μm^2, $k_{ao} = 10^{-9}$ μm^2); d, P_a as a function of the diameter d and for different ligand-receptor affinities k_{fo} ($S = 100$ sec^{-1} ; $m_r = 10^{+2}$ #/μm^2, $m_l = 10^{+4}$ #/μm^2, k_{ro}=10^{-3} μm^2).